sustainability

MDPI

Article

Thermal Load Analysis of Piston Damaged by Wall-Wetting Combustion in a Heavy-Duty Diesel Engine

Haiying Li [1], Yaozong Li [1], Yanzhao An [2,*], Yi Zhang [3], Zhicheng Shi [4], Weiqing Zhu [1], Yongping Qiang [1] and Ziyu Wang [1]

[1] China North Engine Research Institute, Tianjin 300400, China
[2] State Key Laboratory of Engines, Tianjin University, Tianjin 300072, China
[3] School of Energy and Power Engineering, North University of China, Taiyuan 038507, China
[4] School of Mechanical Engineering, Beijing Institute of Technology, Beijing 100081, China
* Correspondence: yanzhao_an@tju.edu.cn

Abstract: Piston damage is a frequent problem of engine durability and plays an important role in an engine's performance design. Recently, a large amount of piston erosion has occurred in a series of heavy-duty diesel engines. To investigate the reason for the piston erosion, a study of the computational fluid dynamics (CFD) of the combustion process in the cylinder and finite element analysis (FEA) of piston was carried out under different initial temperatures. The results show that when the initial temperature decreases from 380 K to 307 K, the mass of wall-wetting increases by 73%, and the maximum combustion pressure increases from 8.1 MPa to 11 MPa; when the initial temperature decreases from 350 K to 328 K, the highest temperature at the throat of the valve pocket increases by nearly 100 K, doubling the temperature fluctuation; and in the case of 328 K, areas exceeding 700 K are concentrated on the top surface of the piston, and the temperature gradient in the depth direction of the throat position decays rapidly.

Keywords: wall-wetting; computational fluid dynamics; finite element analysis; piston; damage

Citation: Li, H.; Li, Y.; An, Y.; Zhang, Y.; Shi, Z.; Zhu, W.; Qiang, Y.; Wang, Z. Thermal Load Analysis of Piston Damaged by Wall-Wetting Combustion in a Heavy-Duty Diesel Engine. *Sustainability* **2023**, *15*, 14634. https://doi.org/10.3390/su151914634

Academic Editor: Talal Yusaf

Received: 15 August 2023
Revised: 19 September 2023
Accepted: 25 September 2023
Published: 9 October 2023

1. Introduction

With the increase in power density in heavy-duty engines, the cyclic fuel supply significantly increases. However, ignition migration and cyclic variation frequently occur in heavy-duty engines under low-temperature conditions below −30 °C. Under low-temperature conditions, the quality of fuel atomization deteriorates, with a large number of fuel jets hitting walls and an increase in the mass of fuel wall wetting [1].

Therefore, the dynamics of wall films, such as wall film formation, propagation, and breakup, require further investigation. Wall film during spray impinging can be quantitatively measured using laser-induced fluorescence and Mie scattering methods, and film thickness has been measured using low-speed refractive index matching in a constant volume chamber [2,3]. Recently, impinging spray characteristics, including impinging distance, wall angle, wall temperature, injection pressure, and fuel mass, have been fully investigated [4–10]. Adjusting the injection parameters is the common way to improve the fuel atomization quality. Although increasing the injection pressure is conducive to shortening the lifetime of fuel adhesion [3], ignition instability may occur with the increase in injection pressure under the condition of low temperature [8]. Scholars have simulated the characteristics of fuel film formation and spray impinging under cold conditions and the influence and law of spray-wall impinging distance on ignition and combustion morphology in low-temperature environments [11–14].

After spray impinging on the wall, due to the slow evaporation rate of the wall film and the extension of ignition delay, the probability of abnormal combustion such as wall-attached combustion and rough combustion is greatly increased [11,15]. Owing to more combustible mixture prior to ignition, more prominent premixed combustion occurs [16].

The diesel knock was firstly captured by Park et al. [17] using the continuous wavelet-transform technique with the pressure signal analysis and high-speed imaging method on an optical engine under the operating condition of premixed charge-compression ignition combustion. Judging from the signal power spectrum of the in-cylinder pressure trace, violent pressure oscillation occurs, leading to damage or even erosion to the piston crown under high-frequency thermal and mechanical loads of high-temperature gas [18]. Qiang et al. [15] investigated the pressure characteristics of diesel engines in low-temperature environments by adjusting different returning water temperatures on an engine thermal performance bench. They discovered that the phenomenon of rough combustion with an ultra-high pressure rise rate occurs under extremely cold conditions.

Rough combustion leads to concentrated heat release during combustion, resulting in a significant increase in heat flux. The phenomena of impinging spray cooling effect and a sharp heat flux variation with the occurrence of rough combustion in a constant volume combustion chamber were discovered using optical diagnostics, wall temperature measurement, and CFD methods [19,20]. Once the heat flux exceeds the allowable limit of the material, piston erosion may occur [19]. Bao et al. [21] analyzed the micromorphology and macro characteristics of an aluminum silicon alloy material of which the ablated piston is made and pointed out that the thermal load of the piston's top surface is an important cause of the gradual development of microcracks between grain boundaries, further resulting in ablation.

However, there is still a lack of clarity on the effect of wall-attached combustion on the thermal load of pistons. A classical steady-state thermal load analysis has been widely used in the analyses of thermal mechanical fatigue, such as the effects of strength and the deformation of aluminum silicon alloys through tensile and thermal cycling methods [22–27]. But in order to accurately predict the fluctuating thermal load due to rough combustion, it is necessary to carry out a transient temperature calculation for the piston at a small timescale coupled with the instant heat flux variation from in-cylinder gas calculated using the CFD method. Due to the large timescale of FEA, the heat flux and heat transfer coefficient miss the characteristics of their high-frequency variation, leading to distortion in the prediction of the piston temperature.

In order to explain the reason for the frequent piston erosion of a series of heavy-duty engines designed by the China North Engine Research Institute (CNERI) under extremely cold conditions, effects of the initial temperature on the wall-wetting and combustion characteristics were made through the CFD of wall-attached combustion, and then a comparison of the transient temperature variation of the piston was made under a rough and normal combustion condition using the FEA of the piston coupled with the 3D CFD modelling.

2. Methodology

2.1. Models of CFD and Validation

A full-size model of a heavy-duty diesel engine combustion chamber has been built, with consideration of the influence of the clearance between the piston ring, the piston, and the cylinder liner on the spray development. The computational meshes for the CFD of the combustion process in a diesel engine are shown in Figure 1. The basic grid size is set to 2 mm, and level 3 of cone-fixed grid refinement is set up at the zone of the nozzle exit. A method of adapted refinement is set up at the positions where the temperature or velocity gradient of the cell is more than the threshold and the positions near the wall. The minimum mesh size is 0.25 mm, and during the spray and combustion process, the number of grids at most of the time is about 6 million. The maximum time step is 1×10^{-6} s, and the minimum time step is 1×10^{-9} s.

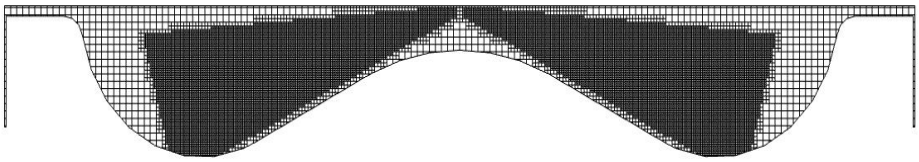

Figure 1. The computational meshes for the CFD of the combustion process in a diesel engine.

The simulation begins at −140 °CA (time of Intake Valve Closing, IVC) and ends at 120 °CA (time of Exhaust Valve Opening, EVO). The main technical parameters and boundary conditions of a heavy-duty diesel engine designed by CNERI [15] are listed in Table 1.

Table 1. The main technical parameters and boundary conditions of CFD.

Content	Value
Compression Ratio	13.5
Flow Coefficient of the Nozzle Hole	0.7
Number of Nozzle Hole	10
Spray Angle	150°
Nozzle Hole Diameter	0.32 mm
Temperature of Cylinder Head	500 K
Temperature of Cylinder Liner	400 K
Temperature of Piston	550 K

The KH and Frossling models were selected for droplet breakup and evaporation, and the NTC collision [28] and Bai–Gosman models [29] were used for the modeling of collision behavior among spray particles and the droplet behavior of impinging sprays, as listed in Table 2. The RNG *k*-ε and SAGE models were chosen for the turbulence and combustion simulation. And a chemical mechanism with four components (named n-C10H22/i-C8H18/C7H14/C7H8) was selected to reproduce the detailed reaction process, which has proven its accuracy in a wide temperature range [30].

Table 2. Sub-model selection for CFD.

Model Type	Name
Droplet Breakup	KH
Droplet Evaporation	Frossling
Droplet Collision	NTC Collision
Droplet Drag	Dynamic droplet drag
Spray-wall Interaction	Wall film
Film Splash	Bai–Gosman
Turbulence	RNG *k*-ε
Combustion	SAGE

The model was validated with the spray behavior of free-jet and wall impinging in a constant-volume chamber and the combustion characteristics in the engine thermal performance bench. As shown in Figure 2a, with the consideration of the uncertainty of experimental results captured using Mie scattering method, the numerical spray-liquid penetration distance achieves a good agreement with the measured results in the constant volume chamber. In terms of in-cylinder pressure during the combustion process under the engine condition, the combustion model was verified with a relative error of ignition delay of 2.8%, and the maximum value of the combustion pressure was 1.3%. More model validations can be found in our previous publications [11,31]. A good agreement of the computational and experimental results has been found.

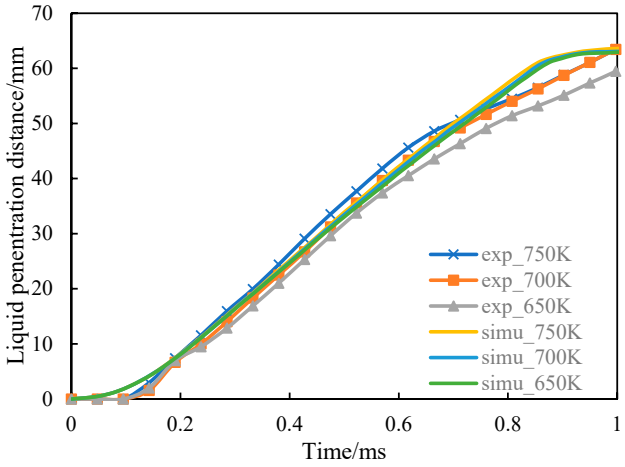

Figure 2. Comparison of numerical and experimental results. (**a**) Free-jet spray-liquid penetration distance under the condition of a constant-volume chamber. (**b**) In-cylinder pressure traces under the condition of a returning water temperature of 15 °C.

2.2. Models of FEA and Validation

To further investigate the effects of wall-wetting combustion and rough combustion under low-temperature conditions on the thermal load of the piston, finite element calculations of the piston temperature were carried out below in the cases of 328 K and 350 K. The finite element calculation is based on a three-dimensional solid model of a prototype piston designed by CNERI using the Pro/E software on the platform of Abaqus. In order to facilitate the analysis, the piston geometric model is appropriately simplified, ignoring oil passages and some small rounded corners. The piston and wear-resistant insert are made of a silicon aluminum alloy and cast-iron materials, respectively. The meshes of the piston and the wear-resistant ring are made of 39,846 grids and 63,911 nodes, as shown in Figure 3.

In order to obtain the boundary conditions for the heat transfer between the piston, the coolant, and the oil, a steady-state heat transfer calculation was initially conducted, which can be validated with the temperature measurement on the engine. The instantaneous traces of the average heat-transfer coefficient and the temperature on the boundary of piston's top land are shown in Figures 4 and 5, respectively.

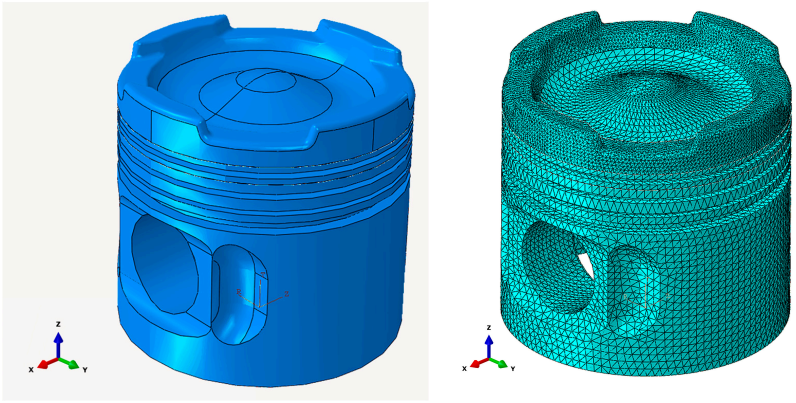

(**a**) (**b**)

Figure 3. Three-dimensional solid and finite element mesh model of the piston. (**a**) Three-dimensional geometric model of the piston. (**b**) Finite element mesh model of the piston.

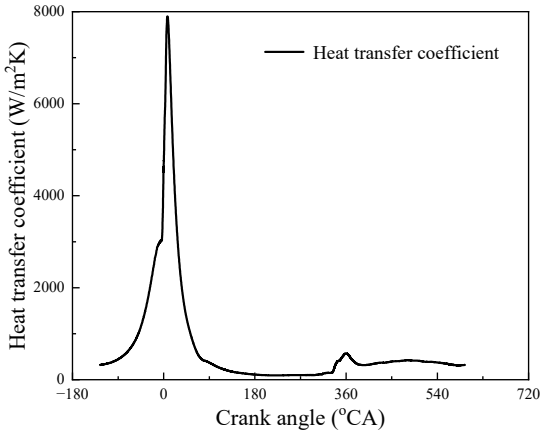

Figure 4. Instantaneous convection heat transfer coefficient of gas.

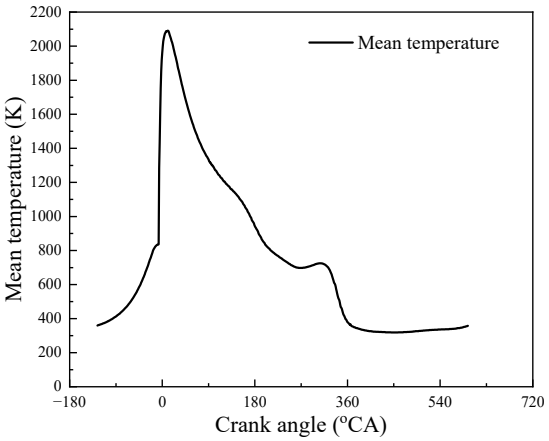

Figure 5. Instantaneous average gas temperature.

To calculate the steady-state temperature of the piston, it is necessary to convert the instantaneous gas temperature and convective heat-transfer coefficient into the average gas temperature T_{gas} and the average convective heat-transfer coefficient α_{gas}, according to Equations (1) and (2):

$$T_{gas} = \frac{\int_0^{\varphi_0} \alpha_g T_g d\varphi}{\int_0^{\varphi_0} \alpha_g d\varphi}, \quad (1)$$

$$\alpha_{gas} = \frac{1}{\varphi_0}\int_0^{\varphi_0} \alpha_g d\varphi \tag{2}$$

where φ is the crank angle and φ_0 represents the crank angle at the final moment.

It is assumed that heat conduction dominates in the area below the first gas ring. For this kind of multi-layer flat wall, the thermal conductivity model is

$$\mathrm{q} = \frac{t_1 - t_{n+1}}{\sum_{i=1}^{n} \frac{\delta_i}{\lambda_i}} = \frac{t_1 - t_{n+1}}{R_i} \tag{3}$$

In the equation, q is the total heat flux; $R_i = \sum_{i=1}^{n} \frac{\delta_i}{\lambda_i}$ is the total thermal resistance; λ_i is the thermal conductivity coefficient of the i-th layer wall; δ_i is the thickness of the i-th layer flat wall; t_1 is the wall temperature of the first layer; and t_n is the wall temperature of the n-th layer. The thermal boundary conditions of the piston top land, piston ring groove, and skirt are determined by the temperature of the cooling water.

The Reynolds number of cooling water in the water jacket $Re = 5.58 \times 10^4$, according to the Dittns–Boelter formula, which calculates the turbulent heat transfer inside the pipe:

$$N_u = 0.023 Re^{0.8} Pr^{0.4}, \tag{4}$$

$$N_u = \frac{\alpha_w D_0}{\lambda_f}, \tag{5}$$

where Nu is the Nusselt number of the cooling water; Pr is the Planck number of the cooling water, $Pr = 5.90$; λ_f is the thermal conductivity of the cooling water, $\lambda_f = 0.68$ W/(m·K); D_0 is the equivalent diameter of the water jacket, D_0 is = 87.8 mm; and α_w is the heat-transfer coefficient between the cylinder liner and the cooling water. As calculated from Equations (4) and (5), $\alpha_w = 2273$ W/(m^2·K).

The piston cavity is cooled through forced fuel injection oscillation cooling, with a heat-transfer coefficient of h_{oil}:

$$h_{oil} = \frac{t_{top} - t_{ca}}{t_{ca} - t_{oil}} \cdot \frac{\lambda}{\delta}, \tag{6}$$

where λ_p is the thermal conductivity of the piston, $\lambda_p = 159$ W/(m·K); δ_p is the thickness of the cavity of the piston crown at the center, $\delta_p = 27.2$ mm; t_{top} is the piston top temperature, $t_{top} = 598$ K; t_{ca} is the piston cavity temperature, $t_{ca} = 573$ K; and t_{oil} is the oil gas temperature under the piston cavity, $t_{oil} = 322$ to 333 K. According to Equation (6), the heat-transfer coefficient of the piston cavity varies among different parts due to the temperature difference between the surface of the piston cavity and the oil, with a value of 582 to 609 W/(m^2·K).

The heat-transfer coefficient of the inner cooling channel is calculated using the Bush empirical formula for the forced oscillation cooling:

$$Nu_c = 0.495 {Re_c}^{0.57} {D_c}^{0.24} {Pr_c}^{0.29}, \tag{7}$$

where the Nusselt number of the oil $Nu_c = \frac{\alpha_c D}{2\lambda_0}$; Reynolds number $Re_c = \frac{(2b/\tau)D\rho}{\mu}$; diameter $D_c = \frac{D_e}{b}$; Prandtl number $Pr_c = \frac{\mu C_P}{\lambda_0}$; average height of the cavity $b = 16 \times 10^{-3}$ m; time required for one revolution of the crankshaft $\tau = 0.04$ s; piston cross-sectional diameter of inner cooling channel $D = 12.7 \times 10^{-3}$ m; density of coolant $\rho = 0.9 \times 10^3$ kg/m^3; dynamic viscosity of coolant $\mu = 0.032$ Pa·s; λ_0 is the thermal conductivity of the oil, $\lambda_0 = 0.128$ W/(m·K); equivalent diameter of the inner cooling channel $D_e = 12 \times 10^{-3}$ m; $D_c = 0.75$; Prandtl number $Pr_c = 500$; and Reynolds number $Re_c = 285.75$. Therefore, the heat-transfer coefficient of the inner cooling channel $\alpha_c = 1418$ W/(m^2·K).

Based on the above finite element model, the steady-state temperature distribution of the piston was calculated, and a comparison with the measured data of the piston was made, as shown in Figure 6. The heat transfer boundary conditions between the piston and

coolant were corrected, and the analysis error of the piston temperature field was controlled within 5% (as shown in Table 3). In summary, the heat transfer boundary conditions between the piston and coolant are shown in Table 4.

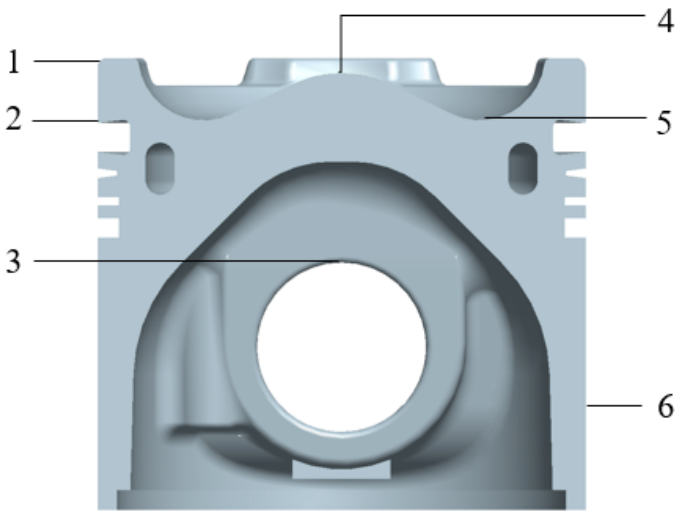

Figure 6. Measurement points for the piston temperature measurement. (1-valve pocket, 2-upper edge of the first ring, 3-upper edge of the pin hole, 4-center, 5-combustion chamber cavity, 6-skirt).

Table 3. Comparison of experimental and numerical temperatures at the measurement points of the piston.

No. of Measurement Point	Experimental Temperature/K	Numerical Temperature/K	Relative Error
1	519	526	1.3%
2	500	503	0.1%
3	489	477	2.5%
4	565	556	1.6%
5	516	506	2.0%
6	374	359	4.3%

Table 4. Boundary conditions of different positions of the piston for the calculation of heat transfer.

Position		Convective Heat Transfer Coefficient/W/(m^2·K)
Top land		148
First ring	Upper edge	311
	Ring groove	67
	Lower edge	1267
	Lower ring land	268
Second ring	Upper edge	466
	Ring groove	120
	Lower edge	466
	Lower ring land	318
Third ring	Upper edge	420
	Ring groove	80
	Lower edge	420
	Lower ring land	79
Fourth ring	Upper edge	459
	Ring groove	56
	Lower edge	459
Skirt		342
Inner cooling channel		1418
Cavity		609

3. Results and Discussions

3.1. CFD in the Cylinder at Different Initial Temperatures

Ignition delay was extended under low-temperature conditions, and the rate of pressure rise and the heat-release rate increased dramatically, which are closely related to the in-cylinder mixing quality of fuel and air. Thus, the modeling of the in-cylinder fuel–air mixing process under different initial in-cylinder temperatures was carried out, with initial and boundary conditions listed in Table 5. These conditions correspond to different intake temperatures of the engine operating at the speed of 1500 r/min and load of 70%. Since the diesel engine adopts a two-stage turbocharger and intercooler before entering the cylinder, the temperature entering the cylinder is regulated by the intercooler. The ambient atmospheric temperature is 283 K. The initial temperature at −140 °CA in the cylinder of 307 K/328 K/350 K/380 K corresponds to the returning water temperature of the intercooler, which is −10 °C, 15 °C, 40 °C and 75 °C, respectively.

Table 5. Initial and boundary conditions of CFD.

Content	Value
Engine speed/rpm	1500
Injection duration/°CA	18.4
Injection timing/°CA	−22
Fuel injection per cycle/mg	203.7
Initial in-cylinder temperature at −140 °CA/K	307/328/350/380
Initial in-cylinder pressure at −140 °CA/MPa	0.147

Due to the deterioration of atomization and evaporation under the condition of low temperature, the spray penetration distance is extended, further spray impinges on the wall, fuel adheres to the wall, and wall film forms. At different initial temperatures in the cylinder, the moment of spray impinging on the wall is almost the same, which is −13.8 °CA. At 10 °CA, the mass of fuel impinging on the wall and adhering to the wall becomes steady for all four cases, as shown in Figure 7a. Table 6 further shows the quantitative results calculated from CFD results: for all cases, the wet-wall rate (the ratio of the mass of fuel film adhering to the wall to the mass of fuel impinging on the wall) is close to or greater than 90%, meaning that most of the fuel spreads or adheres to the piston's top surface once it impinges on the wall, except for a small amount of fuel droplets bouncing or splashing. Compared with the case of 380 K, the mass of fuel adhering to the wall increases by 73% at the initial temperature of 307 K.

Table 6. Mass of fuel adhering to the wall and the wet-wall rate at different initial temperatures in the cylinder.

Initial Temperature in the Cylinder/K	Mass of Fuel Adhering to the Wall/mg	Wet-Wall Rate
307	45.2	99%
328	41.7	97%
350	35.4	93%
380	26.1	88%

Further, due to the increased mass of the premixed gas formed by the extension of ignition delay under the conditions of low in-cylinder initial temperatures, as shown in Figure 7a, once the fuel–air mixture is ignited, more intense combustion and heat release lead to the rapid evaporation of the wall film and further accelerate the heat-release rate during the main combustion period, as shown in Figure 8. As shown in Figure 7b, during the main combustion period, the proportion of mass for evaporation to the total amount of wall film increases significantly at lower initial temperatures in the cylinder, which are 70.7% in the case of 307 K and only 20.7% in the case of 380 K.

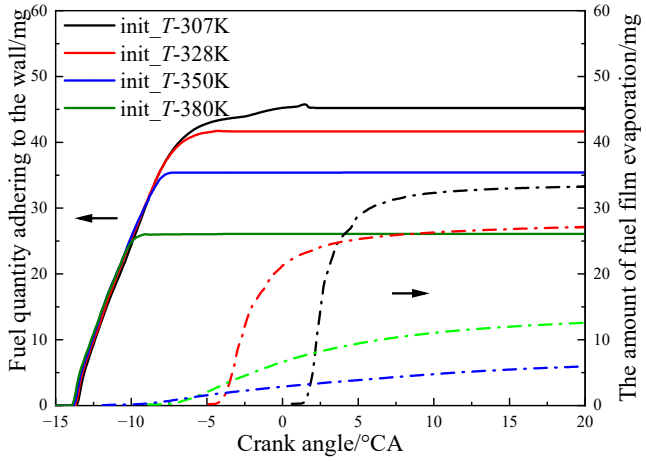

Figure 7. Comparison of the quantity of spray attached and evaporation at different initial temperatures in the cylinder. (**a**) Fuel quantity adhering to the wall and film evaporation. (**b**) Comparison of the proportion of mass for evaporation to the total amount of wall film.

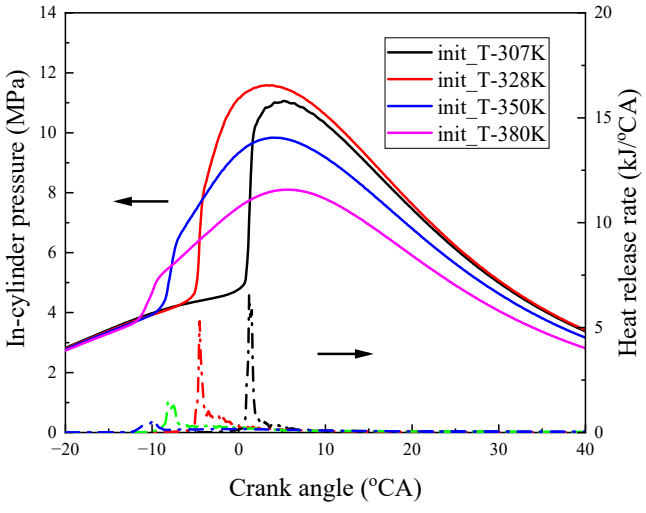

Figure 8. Instantaneous average pressure and heat-release rate in the cylinder at different initial temperatures.

Figure 8 shows the curves of the in-cylinder pressure and the instantaneous heat-release rate under different initial temperatures in the cylinder. It can be seen that as the initial temperature in the cylinder decreases, the ignition delay nonlinearly increases, and the growth amplitude gradually increases. The corresponding combustion starts at the initial temperatures of 380 K, 350 K, 328 K, and 307 K are −12 °CA, −9 °CA, −5 °CA, and 0.5 °CA. The initial temperature in the cylinder decreases from 380 K to 328 K, and the maximum combustion pressure in the cylinder increases from 8.1 MPa to 11.6 MPa. But the maximum combustion pressure in the cylinder decreases to 11 MPa in the case of 307 K. As the initial temperature in the cylinder decreases, the amount of premixed gas formed during the ignition delay significantly increases, especially for the cases of 328 K and 307 K. Therefore, once the mixture ignition occurs, the combustion rate accelerates, the instantaneous heat release rate sharply increases, and the average pressure in the cylinder increases. However, the mixture in the case of 307 K does not ignite until 0.5 °CA. As the ignition occurs, the piston moves downwards, and the combustion chamber volume increases. Therefore, when the initial temperature in the cylinder decreases from 328 K to 307 K, the average pressure in the cylinder slightly decreases.

3.2. FEA of Piston

The numerical results of the steady-state temperature distribution of the piston are shown in Figure 9. The highest temperature appears at the left side of the center of the piston's top surface. This is because the center area of the top surface is close to the high-temperature gas and is far from the cooling channel, resulting in poor heat dissipation. The highest temperature is 558 K, which is at the top land due to the small gap between the piston and the cylinder liner. Having a top land with a relatively high temperature is necessary to prevent the thermal deformation of the piston at the top land from scuffing. The heat of high-temperature gas is gradually transmitted to the piston skirt through the top surface of the piston. The thermal damage to the first ring is commonly caused by the poor lubrication or coking of the lubricating oil. And poor or good lubrication depends on the temperature of the first ring groove. The temperature of the first ring groove is about 485 K, which is lower than the coking temperature of the lubricating oil, which is 503 K. The temperature nonlinearly decreases from the first ring to the skirt with variations in the piston structure and ambient temperature. The inner channel is cooled by oil, dissipating most of the heat from the piston chamber, with a maximum temperature of approximately 506 K. As shown in Figure 9b, the highest temperature is located at both the center and the edge of the combustion chamber pit at the top of the piston. The overall temperature at the top of the left piston is higher than that on the right side. The lowest temperature is located above the inner cooling channel. The temperature difference in the piston ring groove is relatively high, about 11 K to 72 K. The temperature difference between the upper and lower ring areas of the first ring is over 72 K. Although the structure here has been changed to wear-resistant cast iron inserts, the large temperature difference should also be taken seriously to prevent heat accumulation from causing thermal damage to the first ring.

Based on the steady-state finite element calculation of the piston's temperature, transient finite element analyses of the piston's temperature were conducted. The diesel engine operates at a 70% load with a engine speed of 1500rpm. Thus, the time required for one working cycle is 0.008 s. The instantaneous gas temperatures and heat transfer coefficient are calculated via the CFD between the gas, and the piston wall is averaged in individual durations of −125–−4 °CA, −4–4 °CA, 4–14 °CA, and 14–100 °CA and mapped to the piston surface.

The mapping boundary conditions of each duration in the case of 350 K are shown in Figure 10. They were obtained via the CFD results during the combustion process in the cylinder, and a Fourier amplitude function was applied in the other processes, which were divided into three stages, 100–230 °CA, 230–362 °CA, and 362–595 °CA. The average temperature and average heat-transfer coefficient of the gas applied in these three

stages were 1014.4 K and 150.0 W/(m^2·K), 668.5 K and 179.4 W/(m^2·K), 335.3 K and 379.2 W/(m^2·K), respectively.

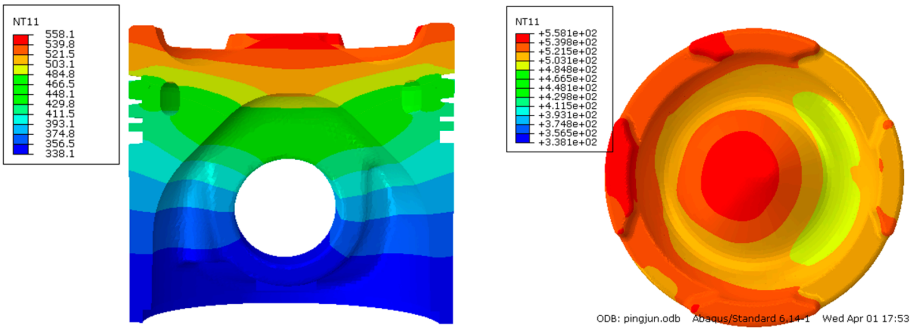

(**a**) Axial distribution (**b**) Radial distribution

Figure 9. Steady-state temperature distribution of the piston.

Based on the numerical results of the steady-state temperature of the piston, five cycles of transient temperature of the piston were calculated, and four of them are illustrated in Figure 11. The instant temperature carves at five positions are illustrated in Figure 10, which are the maximum of the temperature, the center of the piston, the valve pocket, a 0.5 mm depth, and a 1 mm depth under the valve pocket. The piston temperature distribution at each crank angle is shown in Figure 12.

It can be seen that the highest temperature locates on the top surface of the piston where is close to the center of the piston, with a maximum temperature of 615.91 K and a temperature fluctuation amplitude of 20.50 K. The maximum temperature at the center of the piston is 607.51 K, with a temperature fluctuation amplitude of 11.38 K. The second peak of temperature locates at the valve pocket, with a maximum temperature of 610.45 K and a temperature fluctuation amplitude of 20.75 K. At a depth of 0.5 mm, the highest temperature is 597.33 K, with a temperature fluctuation amplitude of 7.63 K and a delay of 24 °CA compared with the top surface; at a depth of 1 mm, the highest temperature is 595.51 K, with a temperature fluctuation amplitude of 5.81 K and a delay of 118 °CA compared with the top surface.

The instantaneous temperature of the gas and the distribution of the heat transfer coefficient between the gas and the piston calculated from Converge ™ indicate that the high-temperature heat release begins on the right side, then a rapid heat release occurs in the cylinder, and finally, in the post-combustion stage, the high temperature is concentrated on the lower right side, with a temperature significantly higher than that in the other regions, as shown in Figure 13.

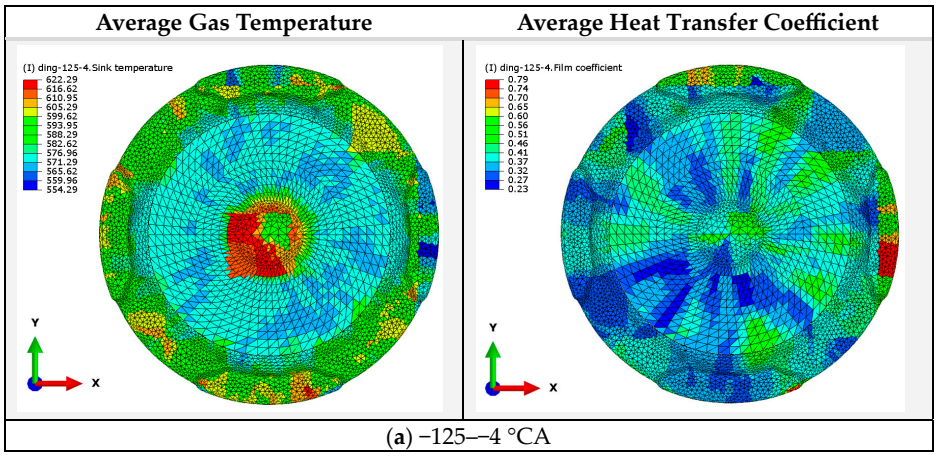

(**a**) −125–−4 °CA

Figure 10. *Cont.*

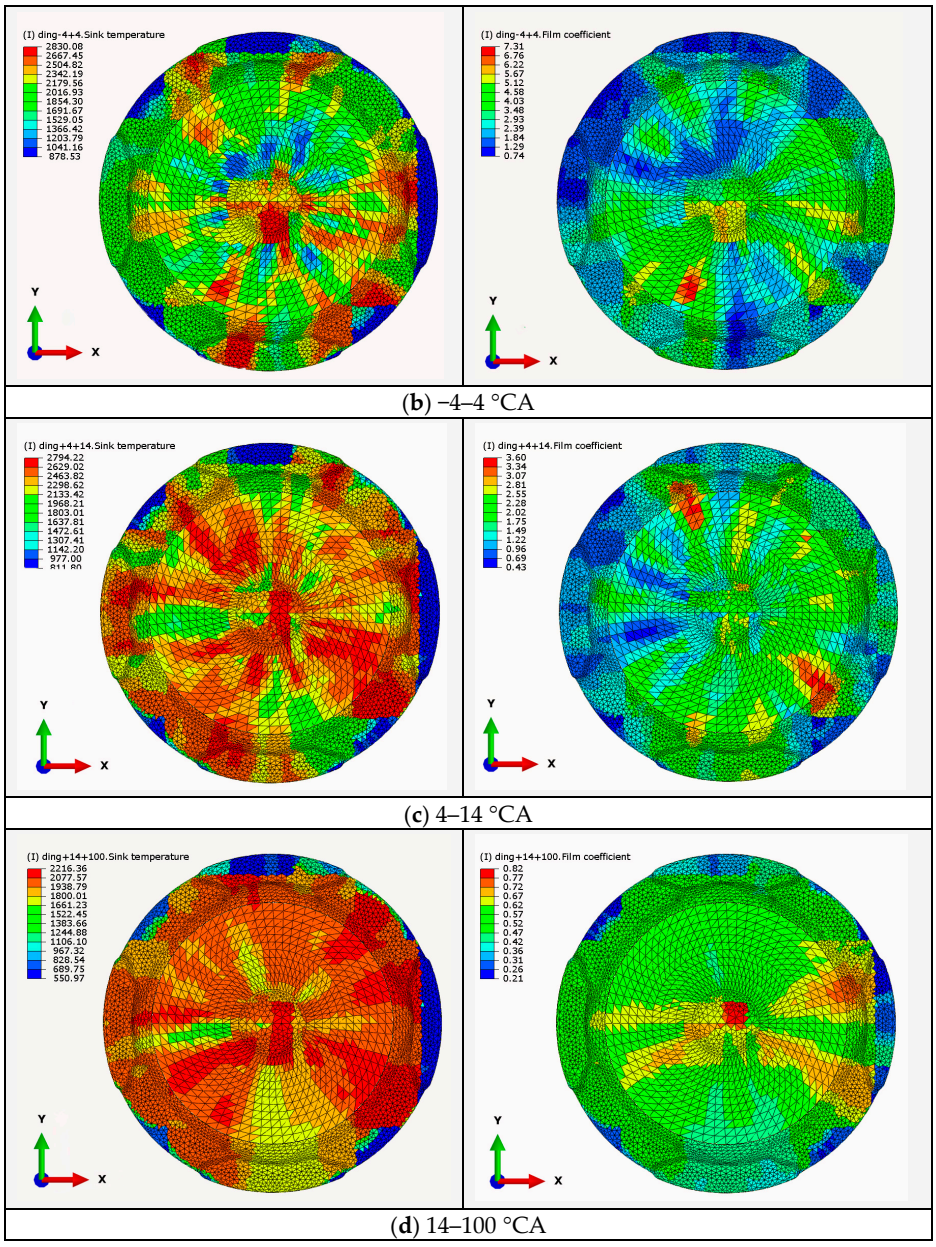

Figure 10. Mapping of average temperature and heat-transfer coefficient in the case of 350 K.

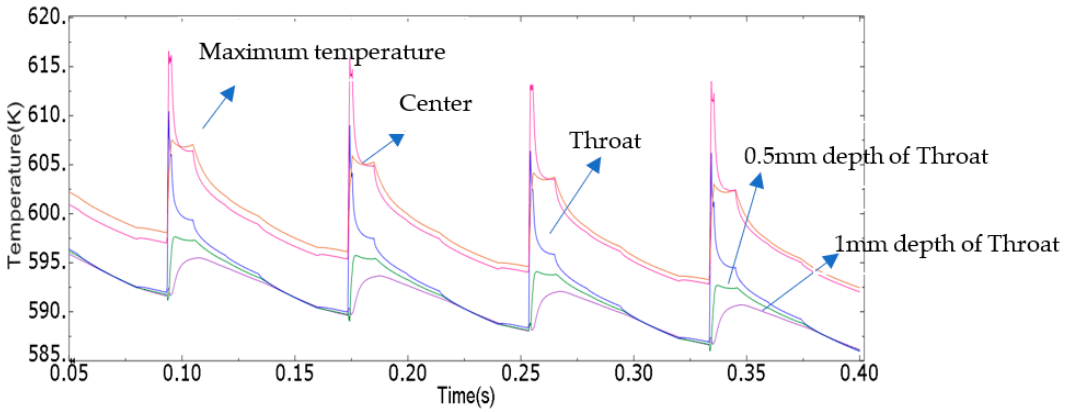

Figure 11. Instant temperature on the top surface of the piston during the working cycle in the case of 350 K.

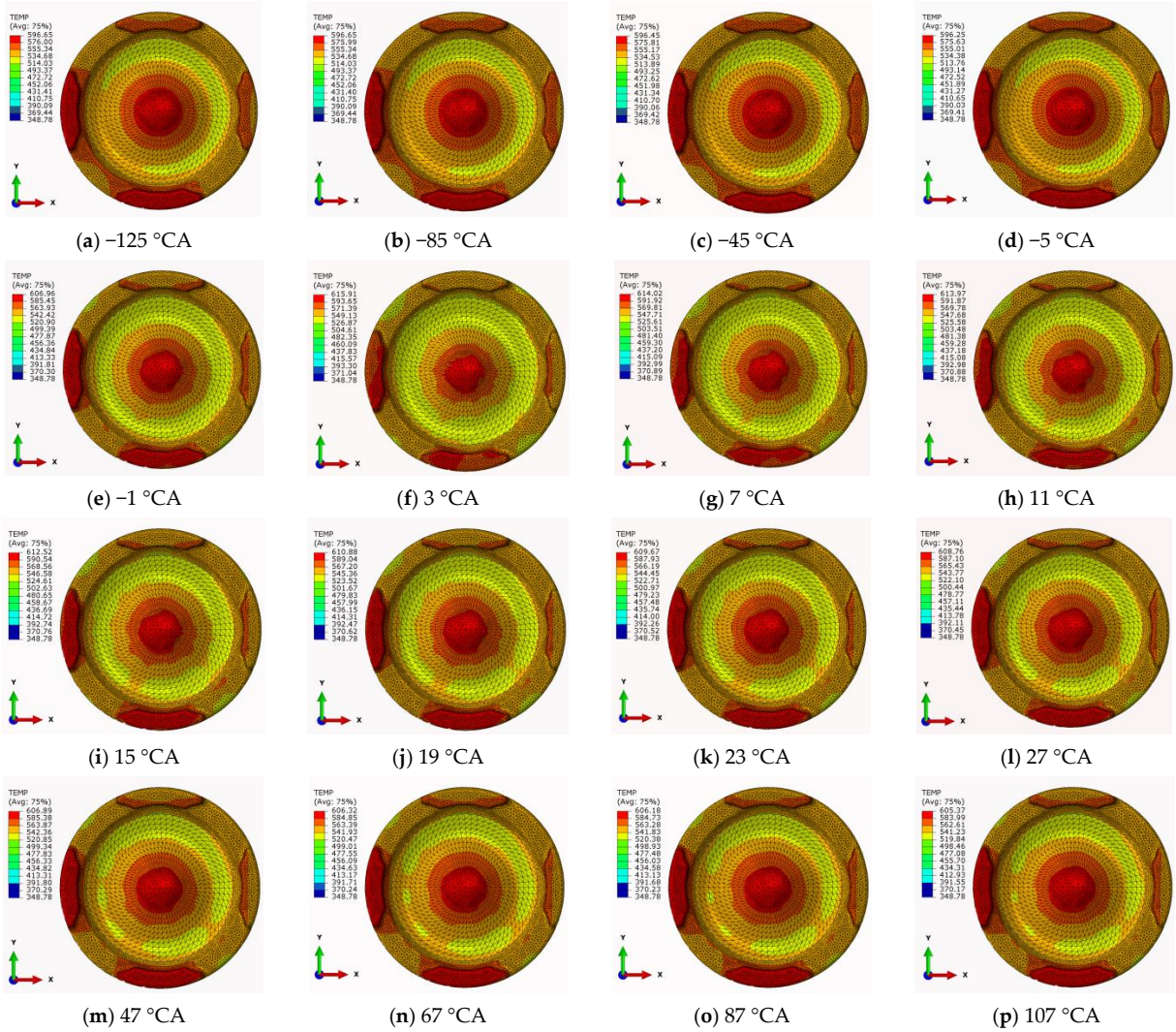

(**a**) −125 °CA (**b**) −85 °CA (**c**) −45 °CA (**d**) −5 °CA

(**e**) −1 °CA (**f**) 3 °CA (**g**) 7 °CA (**h**) 11 °CA

(**i**) 15 °CA (**j**) 19 °CA (**k**) 23 °CA (**l**) 27 °CA

(**m**) 47 °CA (**n**) 67 °CA (**o**) 87 °CA (**p**) 107 °CA

Figure 12. Temperature distribution of the piston's top surface in the case of 350 K.

The instantaneous temperature of five positions in the case of 328 K, which are the maximum temperature, the center of the piston, the valve pocket, the 0.5 mm depth, and the 1 mm depth under the valve pocket, are shown in Figure 14, and the piston temperature distribution at each crank angle is shown in Figure 15.

It can be seen that in the case of 328 K, the highest temperature is located at the throat of the valve pocket, with a maximum temperature of 708.19 K and a temperature fluctuation amplitude of 51.49 K. The maximum temperature at the center of the piston is 654.90 K, with a temperature-fluctuation amplitude of 10.84 K. At a depth of 0.5 mm under the throat of the valve pocket, the highest temperature is 674.13 K, with a temperature-fluctuation amplitude of 17.43 K and a delay of 14 °CA compared with the top surface; at a depth of 1 mm, the highest temperature is 667.15 K, with a temperature fluctuation-amplitude of 10.45 K and a delay of 114 °CA compared with the top surface.

Table 7 compares the maximum temperature and temperature fluctuations at similar locations for the cases of 328 K and 350 K in the cylinder. When the initial temperature in the cylinder decreases from 350 K to 328 K, firstly, the highest temperature at the throat increases by nearly 100 K, and the temperature fluctuation amplitude doubles. Secondly, the highest temperature at the center increased by 47.39 K, and the temperature-fluctuation amplitude remained almost the same. Furthermore, the temperature difference from the throat of the valve pocket to a depth of 0.5 mm increases from 13.12 K to 34.06 K, with an increase of 1.6 times. This indicates a significant increase in the temperature gradient along

the depth direction. Finally, the temperature difference from 0.5 mm to 1 mm is below 10 K. This indicates that the high temperature in the case of 328 K is concentrated on the surface of the piston, and the temperature gradient in the depth direction of the throat decays rapidly.

Table 7. Comparisons of maximum temperature and temperature-fluctuation amplitude at similar positions with different initial temperatures.

Position	Initial Temperature of 328 K		Initial Temperature of 350 K	
	Maximum of Temperature	Amplitude of Temperature Fluctuation	Maximum of Temperature	Amplitude of Temperature Fluctuation
Throat of valve pocket	708.19 K	51.49 K	610.45 K	20.75 K
center	654.90 K	10.84 K	607.51 K	11.38 K
0.5 mm depth of the throat of valve pocket	674.13 K	17.43 K	597.33 K	7.63 K
1 mm depth of the throat of valve pocket	667.15 K	10.45 K	595.51 K	5.81 K

It is noticeable that the highest temperature crankshaft angle is 15 °CA, reaching a temperature of 708.19 K in the case of 328 K, as shown in Figure 15. The position with a temperature exceeding 700 K is located at the throat of the top surface of the piston. For thermal mechanical fatigue, when the maximum temperature exceeds 700 K, the creep and micro-plastic deformation become more severe, such that it is easy for microvoids combined with the creep to form. The microcracks around the interface near the matrix are formed from the coalescence of microvoids under the fatigue loading and finally deboned along the interface [21]. These characteristics of the material can be visualized using the sectional morphology and energy-dispersive spectroscopy in an ablated piston, as shown in Figure 16. The related material analyses have been performed in a previous publication [21].

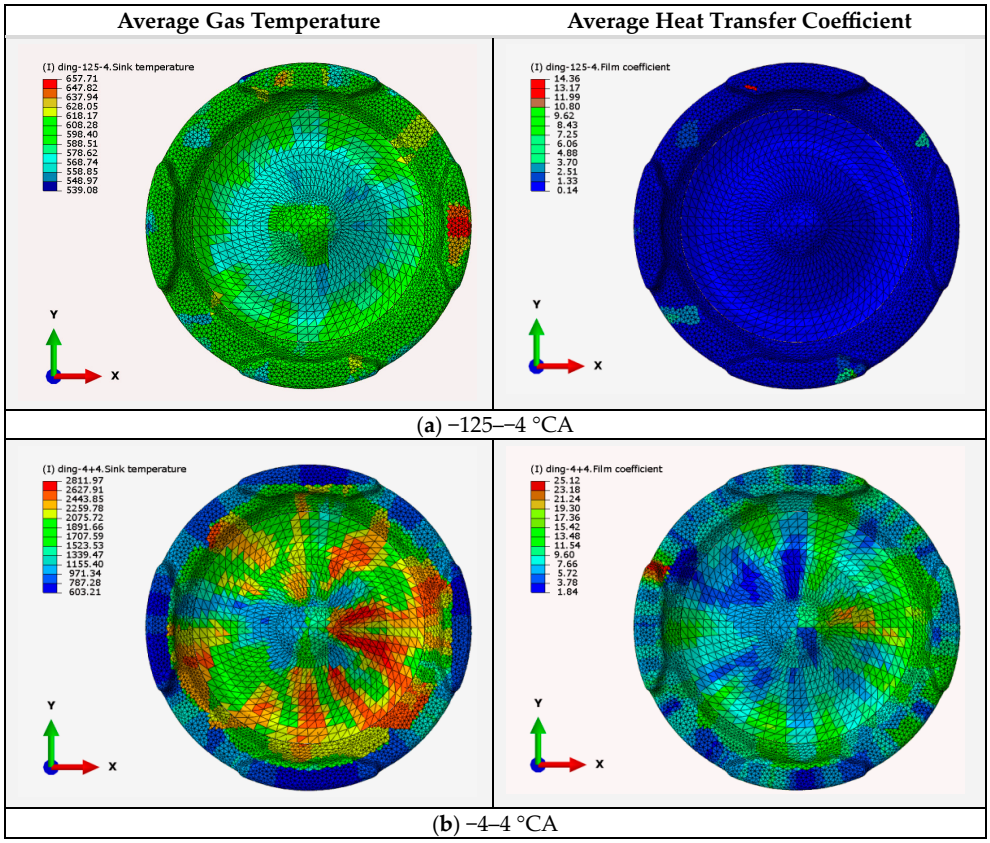

Figure 13. *Cont.*

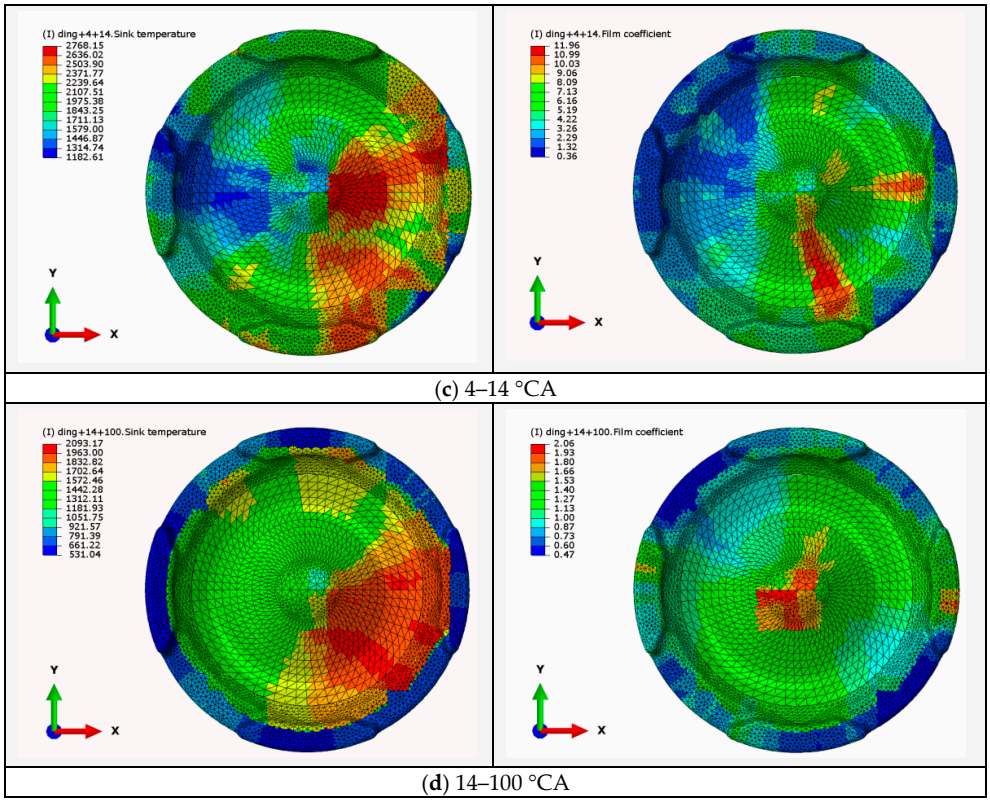

Figure 13. Mapping of average temperature and heat-transfer coefficient in the case of 328 K.

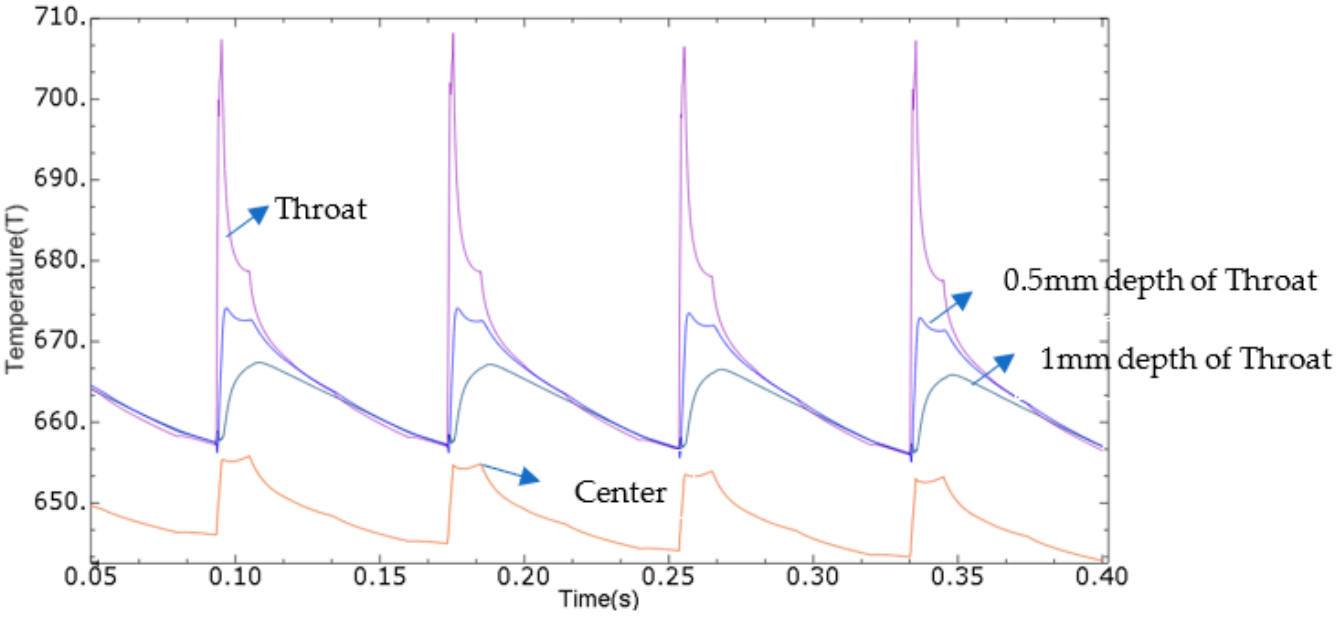

Figure 14. Instant temperature on the top surface of the piston during the working cycle in the case of 328 K.

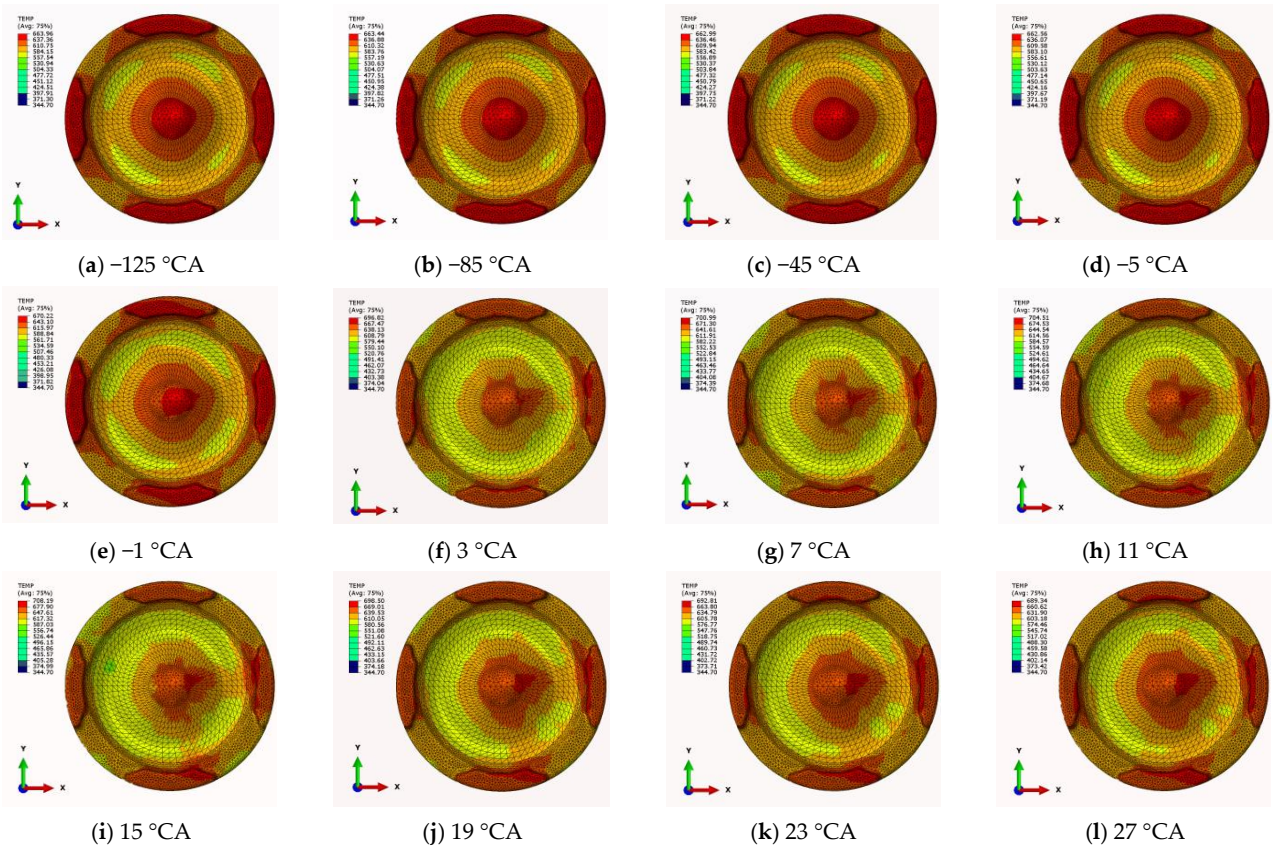

(**a**) −125 °CA (**b**) −85 °CA (**c**) −45 °CA (**d**) −5 °CA

(**e**) −1 °CA (**f**) 3 °CA (**g**) 7 °CA (**h**) 11 °CA

(**i**) 15 °CA (**j**) 19 °CA (**k**) 23 °CA (**l**) 27 °CA

Figure 15. Temperature distribution of the piston's top surface in the case of 328 K.

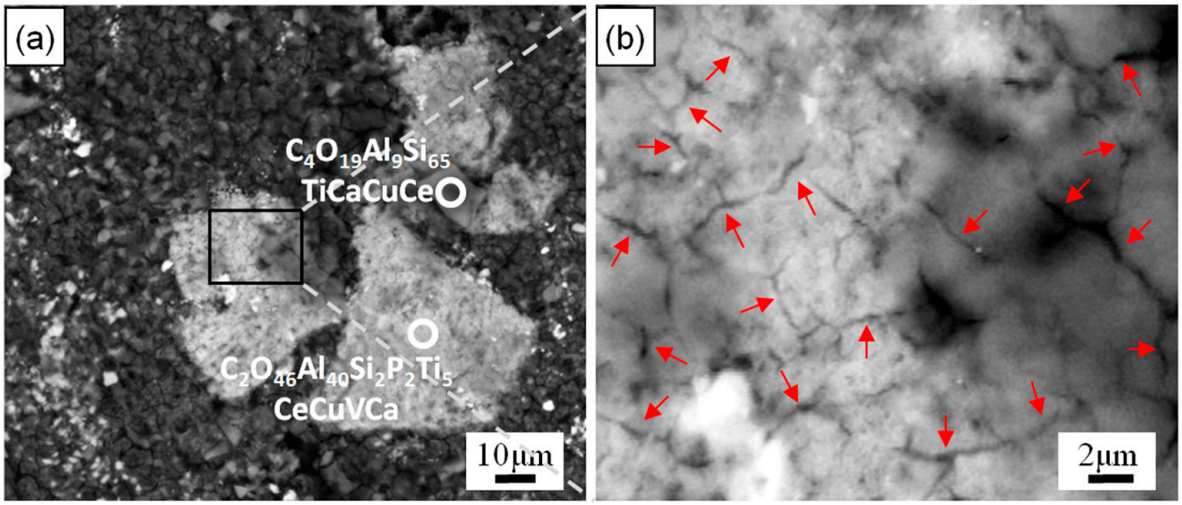

Figure 16. Sectional morphology and energy dispersive spectroscopy in an ablated piston (reprinted from [21]). (**a**) Sectional morphology. (**b**) energy dispersive spectroscopy (arrow indicates the positions of microvoids).

4. Conclusions

In this paper, the analyses of spray impinging and film evaporation and the combustion characteristics for the wall-attached combustion under different initial temperatures in the cylinder were made using a validated CFD model. And an analysis of the piston's thermal load was performed using FEA through mapping from the average gas temperature and

heat-transfer coefficient on the boundary of the piston from the CFD results. The main conclusions of this study are summarized as follows.

(1) Under the condition of operating at a 70% load and an engine speed of 1500 rpm, most of the fuel is spread or adheres to the piston surface once it impinges on the wall, except for a small amount of fuel droplets bouncing or splashing. When the initial temperature decreases from 380 K to 307 K, the mass of wall wetting increases by 73%, and the proportion of mass for evaporation to the total amount of wall film increases from 20.7% to 70.7%.

(2) As the initial temperature in the cylinder decreases, the ignition delay nonlinearly increases, and the growth amplitude gradually increases. The corresponding combustion starts at the initial temperatures of 380 K, 350 K, 328 K, and 307 K are −12 °CA, −9 °CA, −5 °CA, and 0.5 °CA. When the initial temperature in the cylinder decreases from 380 K to 328 K, the maximum combustion pressure in the cylinder increases from 8.1 MPa to 11.6 MPa.

(3) With respect to the steady-state temperature distribution of the piston, firstly, the FEAs have been validated using the temperature measurement on the engine. The overall temperature at the top of the left piston is higher than that on the right side. The lowest temperature locates the position above the inner cooling channel, which is 506 K. And the highest temperature appears at the left of the center of the piston's top surface, and it is 558 K. The temperature difference in the piston's ring groove is relatively high, about 11 K to 72 K.

(4) With regard to the small-scale FEA, a comparison of the transient temperature distribution of the piston was made for the initial temperature of 350 K and 328 K. In the case of the initial temperature of 350 K, the highest temperature is located on the top surface of the piston, which is close to the center of the piston, with a maximum temperature of 615.91 K and a temperature fluctuation amplitude of 20.50 K. In the case of the initial temperature of 328 K, the highest temperature is located at the throat of the valve pocket, with a maximum temperature of 708.19 K and a temperature fluctuation amplitude of 51.49 K, which doubles the temperature fluctuation in the case of 350 K. This is because, due to the typical wall-attached and rough combustion that occurs, the high temperature is concentrated on the valve pocket of piston top surface.

(5) When the maximum temperature exceeds 700 K, the probability of a severe thermal mechanical fatigue increases greatly resulting from the creep and micro-plastic deformation. In the case of the initial temperature of 328 K, the areas exceeding 700 K are concentrated on the top surface of piston, and the temperature gradient decays rapidly along the depth direction of the throat position.

Author Contributions: Conceptualization, H.L. and Y.A.; methodology, Y.L. and H.L.; validation, Z.S. and H.L.; formal analysis, W.Z.; investigation, Y.Z. and H.L.; resources, W.Z., Z.S., Y.Z. and Y.Q.; data curation, Y.Q.; writing—original draft preparation, H.L.; writing—review and editing, H.L., Y.A., Z.S. and Y.Z.; visualization, H.L.; supervision, H.L., Y.A. and Z.W. All authors have read and agreed to the published version of the manuscript.

Funding: This study is financially supported by the Foundation of State Key Laboratory of Engines (No. K2022-12).

Institutional Review Board Statement: Not applicable.

Informed Consent Statement: Not applicable.

Data Availability Statement: Not applicable.

Conflicts of Interest: The authors declare no conflict of interest.

Nomenclature

A	Heat-transfer coefficient
D	Diameter
δ	Thickness
λ	Thermal conductivity
μ	Dynamic viscosity
Nu	Nusselt number
Pr	Planck number
q	Heat flux
Re	Reynolds number

Abbreviations

CFD	Computational Fluid Dynamics
CNERI	China North Engine Research Institute
EVO	Exhaust Valve Opening
FEA	Finite Element Analysis
IVC	Intake Valve Closing

References

1. Liu, F.; Yang, Z.; Li, Y.; Wu, H. Experimental study on the combustion characteristics of impinging diesel spray at low temperature environment. *Appl. Therm. Eng.* **2019**, *148*, 1233–1245. [CrossRef]
2. Li, X.; Xiao, D.; Parrish, S.E.; Grover, R.O., Jr.; Hung, D.L.; Xu, M. Dynamics of spray impingement wall film under cold start conditions. *Int. J. Engine Res.* **2020**, *21*, 319–329. [CrossRef]
3. Zhang, G.; Shi, P.; Dong, P.; Zhang, F.; Zhang, Y.; Luo, H. Experimental Study on the Adhesive Fuel Features of Inclined Wall-Impinging Spray at Various Injection Pressure Levels in a Cross-Flow Field. *Sustainability* **2023**, *15*, 6312. [CrossRef]
4. Zhang, Z.; Liu, F.; An, Y.; Gao, H.; Du, W.; Gao, Y.; Lou, J. Effect of wall surface temperature on ignition and combustion characteristics of diesel fuel spray impingement. *Appl. Therm. Eng.* **2018**, *137*, 47–53. [CrossRef]
5. Wang, Z.; Li, Y.; Wang, C.; Xu, H.; Wyszynski, M.L. Near-nozzle microscopic characterization of diesel spray under cold start conditions with split injection strategy. *Fuel* **2016**, *181*, 366–375. [CrossRef]
6. Wang, Z.; Jiang, C.; Xu, H.; Wyszynski, M.L. Macroscopic and microscopic characterization of diesel spray under room temperature and low temperature with split injection. *Fuel Process. Technol.* **2016**, *142*, 71–85. [CrossRef]
7. Hwang, J.; Park, Y.; Kim, K.; Lee, J.; Bae, C. Improvement of diesel combustion with multiple injections at cold condition in a constant volume combustion chamber. *Fuel* **2017**, *197*, 528–540. [CrossRef]
8. Chen, H.; Shi, Z.; Liu, F.; Wu, Y.; Li, Y. Non-monotonic change of ignition delay with injection pressure under low ambient temperature for the diesel spray combustion. *Energy* **2022**, *243*, 123017. [CrossRef]
9. Chen, B.; Feng, L.; Wang, Y.; Ma, T.; Liu, H.; Geng, C.; Yao, M. Spray and flame characteristics of wall-impinging diesel fuel spray at different wall temperatures and ambient pressures in a constant volume combustion vessel. *Fuel* **2018**, *235*, 416–425. [CrossRef]
10. Nawi MA, M.; Kidoguchi, Y.; Izamshah, R.; Kasim, M.S.; Khor, C.Y.; Jamalludin, M.R.; Rahim, W.M.F.W.A.; Rosli, M.U. Observation on dynamic behavior of droplets evaporation after the end-of-injection of diesel spray. In *Green Design and Manufacture: Advanced and Emerging Applications, Proceedings of the 4th International Conference on Green Design and Manufacture, Ho Chi Minh, Vietnam, 29–30 April 2018*; AIP Publishing: Long Island, NY, USA, 2018. [CrossRef]
11. Shi, Z.; Cao, W.; Wu, H.; Li, H.; Zhang, L.; Bo, Y. Research on destructive knock combustion mechanism of heavy-duty diesel engine at low temperatures. *Combust. Sci. Technol.* **2022**, 1–24. [CrossRef]
12. Wang, D.; Shi, Z.; Yang, Z.; Chen, H.; Li, Y. Numerical study on the wall-impinging diesel spray mixture formation, ignition, and combustion characteristics in the cylinder under cold-start conditions of a diesel engine. *Fuel A J. Fuel Sci.* **2022**, *317*, 123518. [CrossRef]
13. Wei, D.; Jinchi, H.; Yifeng, A. Effect of Wall Temperature on Mass Distribution of Diesel Spray-Wall Impingement. *Trans. CSICE* **2019**, *37*, 130–138.
14. Wu, Z.; Deng, P.; Han, Z. A numerical study on fuel film and emissions formations during cold start in a diesel engine using an improved spray-wall impingement model. *Fuel* **2022**, *320*, 123898. [CrossRef]
15. Qiang, Y.; Li, H.; Zhang, X.; Cai, Z.; Zhu, W.; Li, Y.; Gong, Y. Experimental research on effect of return water temperature on the combustion progress in a diesel engine. *Acta Armamentarii* **2020**, *41*, 222–230.
16. Mattson, J.M.; Depcik, C. *Comparison of Engine Operational Modes with Respect to Compression Ignition Engine Knock*; SAE Technical Paper 2018-01-0219; SAE: Warrendale, PA, USA, 2018. [CrossRef]
17. Park, S.S.; Jung, Y.; Bae, C. Diesel Knock Visualization and Frequency Analysis of Premixed Charge Compression Ignition Combustion with a Narrow Injection Angle. *Asia Pac. J. Environ. Law* **2013**, *4*, 1–24. [CrossRef]
18. Cavina, N.; Rojo, N.; Ceschini, L.; Balducci, E.; Poggio, L.; Calogero, L.; Cevolani, R. Investigation of Knock Damage Mechanisms on a GDI TC Engine. In Proceedings of the 13th International Conference on Engines & Vehicles, Capri, Italy, 10–14 September 2017.

19. Nakata, M.; Iwamoto, S.; Masuda, H.; Matsumura, E.; Senda, J. A Study on the Wall Heat Loss from Diesel Spray Flame with Rapid Compression and Expansion Machine. In Proceedings of the International Symposium on Diagnostics and Modeling of Combustion in Internal Combustion Engines, Okayama, Japan, 25–28 July 2017; Volume 9, p. A208. [CrossRef]
20. Kawanabe, H.; Komae, J.; Ishiyama, T. Analysis of flow and heat transfer during the impingement of a diesel spray on a wall using large eddy simulation. *Int. J. Engine Res.* **2019**, *20*, 758–764. [CrossRef]
21. Bao, T.; Li, J.; Liu, L.; Li, H.; Yang, Z.; Guo, Y.; Xia, F.; Yang, W.; Tao, D.; Zheng, J. Evolution of Al-Si-Cu alloy in piston of diesel engine during knock damage. *Eng. Fail. Anal.* **2020**, *112*, 104501. [CrossRef]
22. Wang, M.; Pang, J.C.; Liu, H.Q.; Li, S.X.; Zhang, M.X.; Zhang, Z.F. Effect of constraint factor on the thermo-mechanical fatigue behavior of an Al-Si eutectic alloy. *Mater. Sci. Eng.* **2020**, *783*, 139279. [CrossRef]
23. Tang, W.C.; Piao, Z.Y.; Zhang, J.; Liu, S.Y.; Deng, L.J. Effect of trace elements on the pinhole fatigue-resistance of gasoline Al-Si piston alloy. *Eng. Fail. Anal.* **2019**, *108*, 104340. [CrossRef]
24. Krishnankutty, P.; Kanjirathinkal, A.; Joseph, M.A.; Ravi, M. High Cycle Fatigue Properties of near eutectic Al Si Piston Alloy. *Mater. Today Proc.* **2018**, *5*, 8406–8413. [CrossRef]
25. Wang, M.; Pang, J.C.; Li, S.X.; Zhang, Z.F. Low-cycle fatigue properties and life prediction of Al-Si piston alloy at elevated temperature. *Mater. Sci. Eng. A* **2017**, *704*, 480–492. [CrossRef]
26. Floweday, G.; Petrov, S.; Tait, R.B.; Press, J. Thermo-mechanical fatigue damage and failure of modern high performance diesel pistons. *Eng. Fail. Anal.* **2011**, *18*, 1664–1674. [CrossRef]
27. Wang, M.; Pang, J.C.; Zhang, M.X.; Liu, H.Q.; Li, S.X.; Zhang, Z.F. Thermo-mechanical fatigue behavior and life prediction of the Al-Si piston alloy. *Mater. Sci. Eng. A* **2018**, *715*, 62–72. [CrossRef]
28. Schmidt, D.P.; Rutland, C.J. A new droplet collision algorithm. *J. Comput. Phys.* **2000**, *164*, 62–80. [CrossRef]
29. Bai, C.; Gosman, A.D. Development of Methodology for Spray Impingement Simulation. *SAE Trans.* **1995**, *104*, 550–568.
30. Chang, Y.C.; Jia, M.; Li, Y.P.; Liu, Y.D.; Xie, M.Z.; Wang, H.; Reitz, R.D. Development of a skeletal mechanism for diesel surrogate fuel by using a decoupling methodology. *Combust. Flame* **2015**, *162*, 3785–3802. [CrossRef]
31. Li, H.; Zhang, X.; Li, C.; Cao, R.; Zhu, W.; Li, Y.; Liu, F.; Li, Y. Numerical Study of Knocking Combustion in a Heavy-Duty Engine under Plateau Conditions. *Energies* **2022**, *15*, 3083. [CrossRef]